DOI: 10.13009/EUCASS2019-91

8TH EUROPEAN CONFERENCE FOR AERONAUTICS AND AEROSPACE SCIENCES (EUCASS)

DOI: ADD DOINUMBER HERE

Numerical investigation of transpiration cooling in supersonic nozzles

Valentina König[⋆†] *and Siegfried Müller*[⋆] *and Michael Rom*[⋆]
[⋆]*Institut für Geometrie und Praktische Mathematik, RWTH Aachen University*
Templergraben 55, 52056 Aachen, GERMANY
koenig@igpm.rwth-aachen.de · mueller@igpm.rwth-aachen.de· rom@igpm.rwth-aachen.de
[†]Corresponding author

Abstract

This paper deals with the numerical investigation of transpiration cooling. A coolant is injected through a porous material into a supersonic nozzle where it is interacting with a hot gas flow, a mixture of thermally-perfect calorically-imperfect gases. This setting is modeled using two separate solvers for the nozzle flow and the porous medium flow. These are coupled to each other by boundary conditions imposed at the interface. Numerical simulations in 2D are performed using argon as coolant and a 5-species air model. The cooling effect above the sample and in the wake of the sample is analyzed.

1. Introduction

In future space transportation systems, the reduction of heat load at the wall is an important design parameter. Therefore, cooling of rocket thrust chambers or nozzles is still a broad field of research. A promising supplement to the widely used convective wall cooling is the method of transpiration cooling. Here, a coolant is injected through a porous material into a hot gas flow. While it passes the porous wall the coolant absorbs energy and reduces the heat load within the material. When entering the hot gas flow, a cooling film forms and thickens the boundary layer reducing the heat flux of the wall.
In the 1950s Eckert et al.[8] identified the superior characteristics of this active cooling technique. Terry et al.[24] summarized the possibilities of applying these to rocket nozzles. Transpiration cooling experiments for metallic nozzle applications were performed in [13] and numerical simulations for metallic nozzles can be found in.[15]
The development of light-weight permeable high-temperature fiber ceramics, in particular composite carbon/carbon (C/C) materials, investigated for instance by Selzer et al.,[22] led to increased interest in transpiration cooling. Transpiration cooled thrust chambers were investigated by Ortelt et al.[20] or Herbertz et al.[10] Using argon as a coolant experimental investigations of transpiration cooling with ceramic matrix composite (CMC) materials can be found among other species in Langener[16] and Langener et al.[17] at sub- and supersonic speeds. Numerical simulations of subsonic hot gas channel flow exposed to transpiration cooling were conducted by Jiang et al.[12] and more recently by Prokein et al.[21] In,[5] a numerical study comparing air-argon injection into subsonic channel flow with temperatures around 430 K was presented.
In recent work,[6,7,9] transpiration cooling in a subsonic turbulent channel has been investigated numerically using a two-domain approach. The turbulent hot gas channel flow is modeled by the compressible Reynolds-averaged Navier-Stokes (RANS) equations. These are approximated using the adaptive parallel finite volume flow solver Quadflow.[3] The porous medium flow is modeled by the continuity equation, the Darcy-Forchheimer equation and two temperature equations for both fluid and solid material. Here, we apply a parallel finite element solver using the deal.II library.[1] The two models are coupled by interface conditions in a weak sense. This means both solvers are applied alternately where in each iteration the respective solver is converged to a steady state with respect to the boundary conditions at the interface provided by the solution of the other solver. This process is continued until no further changes in both solutions occur.
Currently, experiments using transpiration cooling in a nozzle are set up at the Shock Wave Laboratory (SWL) at RWTH Aachen University. Therefore, in the present work we extend our numerical investigations to transpiration cooling in a supersonic nozzle with rocket-like temperatures and pressure gradients. In contrast to the channel flow, the pressure drops significantly in streamwise direction in a supersonic nozzle. This has a strong effect on the injection of the coolant. Therefore, the length of the cooling film and the reduction of the heat flux downstream of the porous

DOI: 10.13009/EUCASS2019-91

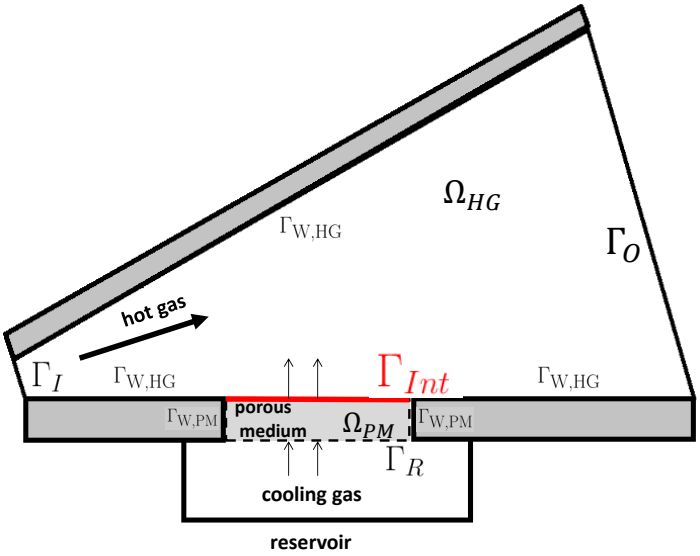

Figure 1: Configuration of coupled fluid-porous medium problem.

material are of special interest. First investigations are performed for a simplified 2D nozzle configuration that is determined as the cross-section of the conical nozzle. Despite the dimensional reduction, the numerical investigations will have impact on the design of the experiment.
The physical model of the porous medium flow and the supersonic nozzle flow with a mixture of thermally perfect gases as well as the coupling of the two solvers are discussed in Sec. 2. In Sec. 3, the numerical method for solving the coupled problem is described. Both the experimental and numerical setup as well as the numerical results are presented in Sec. 4. A summary of the main results and an outlook on future work in Sec. 5 conclude the paper.

2. Physical Model

The configuration for the coupled problem of nozzle flow and porous medium flow is illustrated in Fig. 1. Since the physical model for the porous medium has been discussed in detail in,[6,7,9] we briefly summarize it in Sec. 2.1. In Sec. 2.2 we present (i) the flow equations required to simulate the hot gas flow and (ii) the models applied for the thermodynamic properties. Initial and boundary conditions for both the porous medium and the nozzle flow are given in Sec. 2.3. Finally, the coupling conditions are discussed in Sec. 2.4.

2.1 Porous Medium Flow

In contrast to pure fluids, the porosity φ of the porous material has to be accounted for in the continuum model. It is defined as the ratio of void space to the total volume of the medium. We assume that all void space is connected. Averaging the fluid velocity over a volume V_f consisting only of fluid, the intrinsic average velocity $\vec{V}$ is obtained. This is related to the Darcy velocity $\vec{v}$, i.e., the average velocity with respect to a volume element V_m comprising both solid and fluid material, by the porosity as $\vec{v} = \varphi\vec{V}$.
We are particularly interested in properly capturing transport as well as non-equilibrium temperature effects. Thus, the porous medium model consists of the continuity equation, the Darcy-Forchheimer (momentum) equation and two heat

DOI: 10.13009/EUCASS2019-91

equations:

$$\nabla \cdot \left(\rho_f \mathbf{v}\right) = 0\,, \tag{1a}$$

$$\rho_f \frac{1}{\varphi^2} \left(\mathbf{v} \cdot \nabla\right) \mathbf{v} = -\nabla p - \mu_f \, \mathbf{K_D^{-1}} \mathbf{v} - \rho_f \, \mathbf{K_F^{-1}} |\mathbf{v}| \mathbf{v}\,, \tag{1b}$$

$$0 = (1-\varphi) \nabla \cdot \left(\kappa_s \, \nabla T_s\right) + h \left(T_f - T_s\right), \tag{1c}$$

$$\varphi \rho_f c_{p,f} \frac{1}{\varphi} \mathbf{v} \cdot \nabla T_f = \varphi \nabla \cdot \left(\kappa_f \, \nabla T_f\right) + h \left(T_s - T_f\right). \tag{1d}$$

This system is solved for the variables

$$\mathbf{U}_{PM} = \left(\rho_f, \mathbf{v}, T_s, T_f\right) \tag{2}$$

which denote the fluid density, the Darcy velocity, the solid temperature and the fluid temperature, respectively. In the momentum balance (1b), quadratic drag is included. Here, μ_f denotes the dynamic viscosity of the fluid, $\mathbf{K_D}$ the permeability tensor of the medium and $\mathbf{K_F}$ the Forchheimer permeability coefficient, which is also a tensor. In the simulations presented in this paper, the contribution of the nonlinear Forchheimer term is small. Two heat equations, see (1c) and (1d), are needed since the temperatures T_s of the solid and T_f of the fluid are assumed to be in non-equilibrium. In (1c) and (1d), κ_s and κ_f are the heat conduction coefficients for solid and fluid, respectively and $c_{p,f}$ is the specific heat of the fluid. The exchange of heat between the fluid and the solid is accounted for by the volumetric heat transfer coefficient h to be determined by experiments. The pressure p is determined by the equation of state for a thermally and calorically perfect gas with the specific gas constant R given by

$$p = \rho_f R \, T_f\,. \tag{3}$$

A more detailed discussion of the model can be found in[19] and references cited therein.

2.2 Hot Gas Flow

2.2.1 Governing Equations

Turbulent flows can be described by the Reynolds-averaged Navier-Stokes equations (RANS), which are obtained by applying the Reynolds-averaging

$$f(\mathbf{x},t) = \overline{f}(\mathbf{x},t) + f'(\mathbf{x},t) \qquad \text{with} \qquad \overline{f}(\mathbf{x},t) := \lim_{\Delta \to \infty} \frac{1}{\Delta} \int_t^{t+\Delta} f(\mathbf{x},\tau) d\tau \tag{4}$$

to the compressible Navier-Stokes equations. In contrast to incompressible flows, the resulting equations have a rather complex form due to fluctuations in the density. To simplify the representation, we in addition employ mass-averaging, also referred to as the Favre-averaging

$$f = \widetilde{f} + f'' \qquad \text{with} \qquad \widetilde{f} := \frac{\overline{\rho f}}{\overline{\rho}}\,. \tag{5}$$

In the following, we are using an extended set of the Navier-Stokes equations which accounts for non-reacting mixtures of thermally perfect gases composed of species $\alpha = 1, \ldots, N_s$. Turbulent quantities of the Navier-Stokes equations resulting from the averaging process are modeled via the two-equations Menter SST model:

$$\frac{\partial \overline{\rho}}{\partial t} + \nabla \cdot \left(\overline{\rho} \widetilde{\mathbf{v}}\right) = 0 \tag{6a}$$

$$\frac{\partial \overline{\rho}_\alpha}{\partial t} + \nabla \cdot \left(\overline{\rho}_\alpha \widetilde{\mathbf{v}}\right) = \nabla \cdot \overline{\mathbf{q}}_\alpha^D \tag{6b}$$

$$\frac{\partial (\overline{\rho} \widetilde{\mathbf{v}})}{\partial t} + \nabla \cdot \left(\overline{\rho} (\widetilde{\mathbf{v}} \otimes \widetilde{\mathbf{v}}) + \overline{p} \mathbf{I}\right) = \nabla \cdot \left(\overline{\boldsymbol{\tau}} + \overline{\rho} \tilde{\mathbf{R}}\right) \tag{6c}$$

$$\frac{\partial (\overline{\rho} \widetilde{E})}{\partial t} + \nabla \cdot \left(\widetilde{\mathbf{v}} (\overline{\rho} \widetilde{E} + \overline{p})\right) = \nabla \cdot \left(\overline{\boldsymbol{\tau}} \tilde{\mathbf{v}} - \overline{\mathbf{q}} - \overline{\mathbf{q}}^{\mathbf{t}} - \sum_{\alpha=1}^{N_s} \overline{h}_\alpha \overline{\mathbf{q}}_\alpha^{\mathbf{D}} + \overline{\rho} \tilde{\mathbf{R}} \tilde{\mathbf{v}} \right) + \overline{\rho} D \tag{6d}$$

$$\frac{\partial \left(\overline{\rho} k\right)}{\partial t} + \nabla \cdot \left(\overline{\rho} k \tilde{\mathbf{v}}\right) = P_k - \beta_k \overline{\rho} \omega k + \nabla \cdot \left(\left(\mu + \sigma_k^\star \mu_t\right) \nabla k \right) \tag{6e}$$

$$\frac{\partial \left(\overline{\rho} \omega\right)}{\partial t} + \nabla \cdot \left(\overline{\rho} \omega \tilde{\mathbf{v}}\right) = P_\omega - \beta^\star \overline{\rho} \omega^2 + \nabla \cdot \left(\left(\mu + \sigma_\omega^\star \mu_t\right) \nabla \omega \right) + 2 \left(1 - F_1\right) \frac{\sigma_\omega^0 \overline{\rho}}{\omega} \nabla k \cdot \nabla \omega \tag{6f}$$

DOI: 10.13009/EUCASS2019-91

Since the RANS equations are time-independent, here, t is considered to be a relaxation parameter rather than the physical time. The system (6) is solved for the conservative flow quantities

$$\mathbf{U}_{HG} = \left(\bar{\rho}, \bar{\rho}_\alpha, \bar{\rho}\tilde{\mathbf{v}}, \bar{\rho}\tilde{E}, \bar{\rho}k, \bar{\rho}\omega\right) , \tag{7}$$

which denote the mixture density, the partial densities, the momentum, the total energy, the turbulence kinetic energy and the turbulent dissipation rate, respectively. It is assumed that the flow is frozen, i.e., we do not account for chemical reactions. With N_S denoting the number of species, the system is solved for $N_S - 1$ partial densities $\overline{\rho}_\alpha$, as the density of the remaining specie may be computed from the mixture density

$$\overline{\rho} = \sum_{\alpha=1}^{N_S} \overline{\rho}_\alpha \, . \tag{8}$$

For closure of the system, the pressure $\overline{p}$ is calculated with the equation of state

$$\overline{p} = \sum_{\alpha=1}^{N_S} \overline{p}_\alpha = \sum_{\alpha=1}^{N_S} \overline{\rho}_\alpha R_\alpha \overline{T} \tag{9}$$

with R_α and $\overline{p}_\alpha$ denoting the specific gas constant and the partial pressure of species α, respectively.
The Reynolds stress tensor $\overline{\rho}\tilde{\mathbf{R}}$ is modeled via the Boussinesq hypothesis.[5,25] The laminar energy transport is driven by the thermal conduction $\overline{\mathbf{q}} = \lambda \nabla \overline{T}$. In analogy to Fourier's law, the turbulent heat flux $\overline{\mathbf{q}}^{\mathbf{t}}$ is assumed to be proportional to the temperature gradient such that

$$\overline{\mathbf{q}}^{\mathbf{t}} = -c_P \frac{\mu_t}{Pr_t} \nabla \overline{T} \, . \tag{10}$$

Here, Pr_t is the turbulent Prandtl number. The turbulent viscosity μ_t and the transport term $\overline{\rho}D$ are modeled by the Menter SST turbulence model. Therefore, (6e) and (6f) are solved for the turbulence kinetic energy k and the turbulent dissipation ω. Details on the turbulence model and all related coefficients may be found in the literature, see for instance.[5,18]

2.2.2 Thermodynamic Properties

All required quantities of the gas mixture are computed by considering the corresponding property of each species α and its particular contribution to the gas mixture, e.g., weighted by the mass fraction $X_\alpha = \overline{\rho}_\alpha / \overline{\rho}$. In the present study, a gas mixture of five species air (N, N_2, O, O_2, NO) and the cooling gas argon (AR) are considered.
To determine the total energy

$$\tilde{E} = \frac{1}{2}\tilde{\mathbf{v}}^2 + \sum_{\alpha=1}^{N_S} X_\alpha e_\alpha^0 + \sum_{\alpha=1}^{N_S} X_\alpha e_\alpha(\overline{T}) + k \tag{11}$$

the formation enthalpies e_α^0 and the corresponding internal energies $e_\alpha\left(\overline{T}\right)$ are required. The latter are computed from tabulated data[23] and stored as piecewise polynomials, i.e., a value for the internal energy e_α may be obtained at any relevant and physically meaningful temperature by evaluating the curve fit.
The laminar shear stresses $\overline{\tau}$ are determined by the Newtonian fluid assumption where the effective dynamic viscosity is computed from the laminar and turbulent contributions. The laminar dynamic viscosity μ_l of the gas mixture is calculated applying Wilke's semi-empirical mixing rule. For this purpose, the dynamic viscosity of each species $\mu_{l,\alpha} = \mu_{l,\alpha}(T)$ is computed based on kinetic theory, see for instance the Chapman-Enskog theory.[2] Due to large uncertainties in determining the Lennard-Jones parameters, the data differ depending on which data set is used. To ensure consistency of the data, as much data as possible are used from one of the available data sets.[2,4,11] Note that for the gas mixture computations presented here, the JANAF thermochemical tables[23] are used. The dynamic viscosities of the species $\mu_{l,\alpha}$ are fitted as piecewise polynomials to simplify data handling.[26]
The diffusion flux of each species is approximated by Rick's law

$$\overline{\mathbf{q}}_\alpha^{\mathbf{D}} = -\overline{\rho} D \, \nabla\left(\frac{\overline{\rho}_\alpha}{\overline{\rho}}\right) . \tag{12}$$

This assumption neglects pressure and thermal diffusion and considers only concentration gradients as the driving force. The local single diffusion coefficient D is calculated from the Lewis number, which is defined as $Le = D\rho c_p / \lambda$.

DOI: 10.13009/EUCASS2019-91

For the current configuration, the constant Lewis number for the argon-air combination may simply be approximated from the ratio of the binary diffusion coefficients

$$Le_{ac} = \frac{D_{ac}}{D_{aa}} Le_{aa} \,. \tag{13}$$

The Lewis number Le_{aa} for air is used as a reference value. The binary diffusion coefficients D_{ac} and D_{aa} for air-coolant (ac) mixtures and for air-air (aa) mixtures, respectively, are determined based on the Chapman-Enskog theory. In,[2] approximated Lennard-Jones potential parameters for air mixtures and single species are published.
The transport of enthalpy $\overline{h}_\alpha = e_\alpha(\overline{T}) + R_\alpha \overline{T}$ driven by diffusion also affects the laminar energy transport. The thermal conductivity $\lambda_\alpha = \lambda_\alpha(\mu_\alpha, c_{V,\alpha})$ is calculated by means of the Euken correction for polyatomic molecules.[11] Wilke's semi-empirical mixing rule is applied to determine the mixture conductivity.
For a detailed discussion of the model we refer to.[26]

2.3 Boundary Conditions

For both the nozzle flow and the porous medium flow we have to specify boundary conditions for the boundaries indicated in Figure 1.
At the nozzle entry Γ_I we set freestream values characterizing the nozzle flow: the density ρ_∞, the mass fractions $X_{\alpha,\infty}$ of each species, the temperature T_∞ and the Mach number M_∞. The turbulence kinetic energy is defined by the turbulent intensity $Tu_\infty = \sqrt{2/3\, k_\infty}/v_\infty$, where v_∞ is the velocity component in streamwise direction x. The turbulent dissipation rate ω_∞ is computed by $\rho_\infty k_\infty/\mu_t$, where the ratio of the turbulent dynamic viscosity to the laminar dynamic viscosity $(\mu_t/\mu)_\infty$ is used in combination with the Viscosity Curve Fit model.

To align the nozzle inflow with the centerline, the velocity is inclined by an angle ϕ between the centerline and the x-axis, i.e.,

$$\tilde{v}_{x,\infty} = \cos(\phi) v_\infty, \quad \tilde{v}_{y,\infty} = \sin(\phi) v_\infty \qquad \text{on } \Gamma_\mathrm{I} \,. \tag{14}$$

At the nozzle exit Γ_O only the outflow pressure is prescribed by setting

$$\overline{p} = p_{out} \qquad \text{on } \Gamma_\mathrm{O} \,. \tag{15}$$

The nozzle walls $\Gamma_\mathrm{W,HG}$ are modeled by an adiabatic wall to account for changing wall temperatures. Inside the nozzle, i.e., in the domain Ω_HG, the flow is initialized by a homogeneous state computed from the freestream values.
In the porous medium flow, the temperatures on the boundary Γ_R to the reservoir are determined by

$$T_s = T_b \quad \text{and} \quad T_f = T_c \qquad \text{on } \Gamma_\mathrm{R} \,, \tag{16}$$

where T_b is the temperature of the solid on the adiabatic back side of the porous material and T_c is the coolant temperature in the plenum.
In contrast to previous work[6,7,9] we choose a different boundary condition for the fluid density ρ_f on Γ_R. As the coolant mass flow rate is the physical parameter of interest for the coupling, ρ_f is computed by the ideal gas law such that

$$\rho_f = \frac{p_\mathrm{R,num}}{R\, T_c} \qquad \text{on } \Gamma_R \,, \tag{17}$$

where R denotes the specific gas constant of the coolant, using a fitted reservoir pressure $p_\mathrm{R,num}$ to match the target coolant mass flow as input to the hot gas simulation. We use an outer iteration on the flow solver until the target mass flow rate is met following.[14] In each iteration i, the mass flow rate $\dot{m}^i_\mathrm{Int}$ at the interface Γ_Int is compared with the given target mass flow rate $\dot{m}_c$ and $p_\mathrm{R,num}$ is updated by

$$p^{i+1}_\mathrm{R,num} = p^i_\mathrm{R,num} \, \frac{\dot{m}_c}{\dot{m}^i_\mathrm{Int}} \,. \tag{18}$$

For the first iteration, an initial guess $p^0_\mathrm{R,num}$ is used, e.g., given by an experiment or approximated from the Darcy-Forchheimer equation. The outer iteration ensures the given mass flow rate throughout the entire porous material. Furthermore, the continuity of the pressure distribution at the interface is established.
The side walls of the porous medium denoted by $\Gamma_\mathrm{W,PM}$ are set to be adiabatic, i.e.,

$$\nabla T_s \cdot \mathbf{n} = 0 \,, \quad \nabla T_f \cdot \mathbf{n} = 0 \qquad \text{on } \Gamma_\mathrm{W,PM} \,. \tag{19}$$

DOI: 10.13009/EUCASS2019-91

From a physical point of view, the normal component of $\mathbf{v}$ must vanish on $\Gamma_{\mathrm{W,PM}}$, i.e.,

$$\mathbf{v} \cdot \mathbf{n} = 0 \qquad \text{on } \Gamma_{\mathrm{W,PM}}\,, \tag{20}$$

whereas nontrivial tangential components have to be permitted since no viscous effects are taken into account in the Darcy-Forchheimer momentum equation.
For an initial guess in the porous medium domain Ω_{PM}, suitable values have to be chosen. The density $\rho_{f,0}$ is determined by linearly interpolating the reservoir density and the hot gas density between Γ_{R} and Γ_{Int}, leading to

$$\rho_{f,0}(x,y) = \frac{p_{\mathrm{R,num}}}{R\,T_c} + \frac{y - y_{\mathrm{R}}}{y_{\mathrm{Int}} - y_{\mathrm{R}}} \left(\frac{p_{\mathrm{HG,Int}}}{R\,T_{\mathrm{HG,Int}}} - \frac{p_{\mathrm{R,num}}}{R\,T_c} \right) \qquad (x,y) \in \Omega_{\mathrm{PM}}\,. \tag{21}$$

The normal component $v_{y,0}$ of the Darcy velocity is computed from the target coolant mass flow rate $\dot{m}_c$ and the initial density distribution, i.e.,

$$v_{x,0} = 0\,, \quad v_{y,0} = \frac{\dot{m}_c}{\rho_{f,0} A_c} \qquad \text{in } \Omega_{\mathrm{PM}}\,, \tag{22}$$

where A_c denotes the surface area of the porous material. The back side temperature T_b and the coolant reservoir temperature T_c are used as initial guess for the temperatures such that

$$T_{s,0} = T_b\,, \quad T_{f,0} = T_c \qquad \text{in } \Omega_{\mathrm{PM}}\,. \tag{23}$$

2.4 Coupling Conditions on Γ_{Int}

By alternately applying the flow solver and the porous medium solver, solutions of one solver can be applied to compute boundary conditions for the other solver. Hence, both solvers are coupled and the resulting boundary conditions can be regarded as coupling conditions.
The pressure p_{HG} obtained from the respective hot gas flow solution and the target mass flow rate $\dot{m}_c$ are used to compute the normal component v_y of the Darcy interface velocity at the interface in the porous medium such that

$$v_{y,\mathrm{Int}} = \frac{\dot{m}_c}{\rho_{\mathrm{Int}}\, A_c} \quad \text{with} \quad \rho_{\mathrm{Int}} := \frac{p_{\mathrm{HG}}}{R\,T_f} \qquad \text{on } \Gamma_{\mathrm{Int}}\,. \tag{24}$$

The temperature T_{HG} and the temperature gradient ∇T_{HG} from the hot gas flow solution are applied in the heat flux balance incorporating the solid temperature gradient ∇T_s in the porous medium flow

$$(1-\varphi)\,(\kappa_s \nabla T_s) \cdot \mathbf{n} = c_{p,f}\,\rho_f\,v_{y,\mathrm{Int}}\,(T_f - T_{\mathrm{HG}}) + \kappa_{\mathrm{HG}} \nabla T_{\mathrm{HG}} \cdot \mathbf{n} \qquad \text{on } \Gamma_{\mathrm{Int}}\,, \tag{25}$$

where κ_{HG} denotes the thermal conductivity of the hot gas.
On the other hand, in the hot gas domain Ω_{HG} the velocity $\mathbf{v}_{\mathrm{PM}}$ and the fluid temperature $T_{f,\mathrm{PM}}$ obtained from the porous medium flow solution are used to compute the density $\overline{\rho}$ and the total energy $\tilde{E}$ in the hot gas flow at the interface Γ_{Int}:

$$\overline{\rho} = \frac{\overline{p}}{R_{\mathrm{PM}}\,T_{f,\mathrm{PM}}}\,, \tag{26a}$$

$$\overline{\rho}_\alpha = \overline{\rho}\,X_\alpha\,, \tag{26b}$$

$$\mathbf{v} = \mathbf{v}_{\mathrm{PM}}\,, \tag{26c}$$

$$\tilde{E} = \frac{1}{2}\,\mathbf{v}_{\mathrm{PM}}^2 + \sum_{\alpha=1}^{N_S} X_\alpha e_\alpha^0 + \sum_{\alpha=1}^{N_S} X_\alpha e_\alpha(T_{f,\mathrm{PM}})\,, \tag{26d}$$

$$k = 0\,, \tag{26e}$$

$$\omega = \omega_\infty\,. \tag{26f}$$

Here, the turbulence kinetic energy k is set to zero because the cooling gas injection is assumed to be laminar.

3. Numerical Method

For the solution of the coupled problem, we alternately and approximately solve the compressible RANS equations (6) and the porous medium equations (1) for the hot gas flow and the porous medium flow, respectively. This leads to solutions $\mathbf{U}_{HG}$ and $\mathbf{U}_{PM}$ in the two flow regimes. The iterative process follows
Algorithm:

DOI: 10.13009/EUCASS2019-91

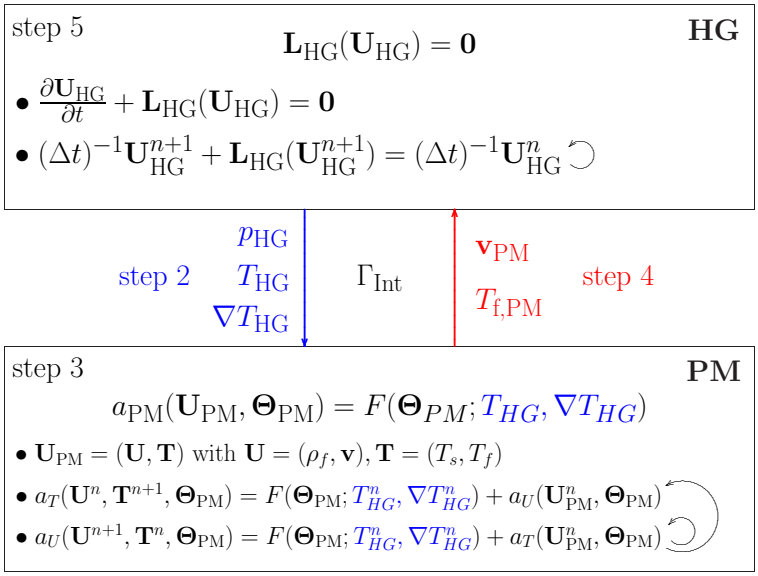

Step 1: Initialize the flow solver.

Step 2: Transfer data $(p_{\mathrm{HG}}, T_{\mathrm{HG}}, \nabla T_{\mathrm{HG}})$ provided by the flow solver to the porous medium solver.

Step 3: Converge the porous medium solver.

Step 4: Transfer data $(\mathbf{v}_{\mathrm{PM}}, T_{f,\mathrm{PM}})$ from the porous medium solver to the flow solver.

Step 5: Converge the flow solver.

Step 6: Perform grid adaptation in the flow solver.

Step 7: Stop if (27) is fulfilled or return to step 2.

The iteration process terminates whenever the stopping criterion

$$\left\| \rho(\mathbf{U}_{HG}^{n+1})\,|_{\Gamma_{Int}} - \rho(\mathbf{U}_{HG}^{n})\,|_{\Gamma_{Int}} \right\|_{\infty} \leq \varepsilon \tag{27}$$

with a prescribed tolerance ε is reached. The steps 2 to 5 of this process are illustrated in Fig. 3 together with additional information on the solution procedure in the respective solver.

The system of equations consisting of the compressible RANS equations using the Menter SST turbulence model is written as $\mathbf{L}_{\mathrm{HG}}(\mathbf{U}_{\mathrm{HG}}) = \mathbf{0}$. Even though we are interested in steady state solutions, we can use the time variable t in the unsteady formulation $\partial \mathbf{U}_{HG}/\partial t + \mathbf{L}_{HG}(\mathbf{U}_{HG}) = \mathbf{0}$ as relaxation parameter in a backward Euler time discretization with the discrete formulation given by

$$(\Delta t)^{-1}\mathbf{U}_{\mathrm{HG}}^{n+1} + \mathbf{L}_{\mathrm{HG}}(\mathbf{U}_{\mathrm{HG}}^{n+1}) = (\Delta t)^{-1}\mathbf{U}_{\mathrm{HG}}^{n}\,, \quad n = 0, 1, 2, \ldots\,. \tag{28}$$

The flow solver Quadflow[3] solves the nonlinear system (28) iteratively by using a fully adaptive cell-centered finite volume method on locally refined grids, see Step 5.

The weak formulation for the porous medium system containing the continuity equation, the Darcy-Forchheimer equation and the two heat equations can be written as

$$a^{\mathrm{PM}}(\mathbf{U}_{\mathrm{PM}}, \mathbf{\Theta}_{\mathrm{PM}}) = F(\mathbf{\Theta}_{\mathrm{PM}};\, T_{\mathrm{HG}}, \nabla T_{\mathrm{HG}})\,, \tag{29}$$

where $a^{\mathrm{PM}}(\mathbf{U}_{\mathrm{PM}}, \mathbf{\Theta}_{\mathrm{PM}})$ is a form that is linear in $\mathbf{\Theta}_{\mathrm{PM}}$ and nonlinear in $\mathbf{U}_{\mathrm{PM}}$. On the right-hand side $F(\mathbf{\Theta}_{\mathrm{PM}};\, T_{\mathrm{HG}}, \nabla T_{\mathrm{HG}})$ is a linear functional. The latter incorporates the coupling condition (25) and therefore depends on T_{HG} and ∇T_{HG}. By applying operator splitting, the vector $\mathbf{U}_{\mathrm{HG}}$ is split into the vectors $\mathbf{U} = (\rho_f, \mathbf{v})$ and $\mathbf{T} = (T_s, T_f)$ such that at first the linear elliptic system

$$a_T(\mathbf{U}^n, \mathbf{T}^{n+1}, \mathbf{\Theta}_{\mathrm{PM}}) = F(\mathbf{\Theta}_{\mathrm{PM}}; T_{\mathrm{HG}}^n, \nabla T_{\mathrm{HG}}^n) + a_U(\mathbf{U}_{\mathrm{PM}}^n, \mathbf{\Theta}_{\mathrm{PM}}) \tag{30}$$

is solved directly. Subsequently the nonlinear hyperbolic system

$$a_U(\mathbf{U}^{n+1}, \mathbf{T}^n, \mathbf{\Theta}_{\mathrm{PM}}) = F(\mathbf{\Theta}_{\mathrm{PM}}; T_{\mathrm{HG}}^n, \nabla T_{\mathrm{HG}}^n) + a_T(\mathbf{U}_{\mathrm{PM}}^n, \mathbf{\Theta}_{\mathrm{PM}}) \tag{31}$$

is solved iteratively in Step 3. For this purpose, a finite element solver has been implemented using the deal.II library.[1] The discretization and the derivation of the weak formulation for the finite element scheme used in the porous medium solver are discussed in detail in.[6,7,9]

DOI: 10.13009/EUCASS2019-91

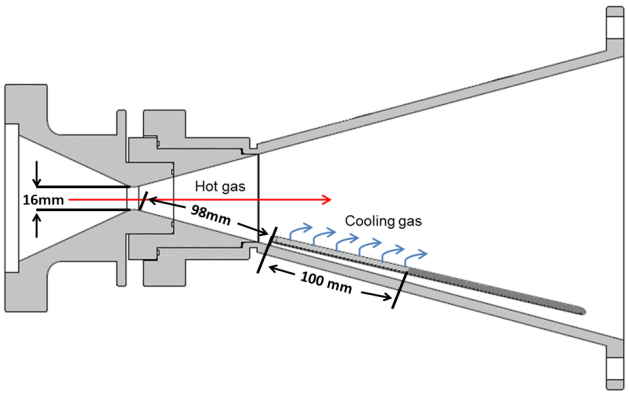

Figure 2: Experimental setup of coupled fluid-porous medium problem (Courtesy of SWL).

Table 1: Hot flow parameters.

stagnation density	ρ_∞	0.92587	kg/m^3
stagnation temperature	T_∞	3486	K
outflow pressure	p_{out}	1000	Pa
Mach number	M_∞	1.01	
turbulent intensity	Tu_∞	0.5	%
viscosity ratio	$(\mu_t/\mu)_\infty$	0.001	
Lewis number	Le	1.2	
Prandtl number	Pr	0.72	

4. Numerical Results

Our numerical investigations are motivated by experiments that will be performed at the Shock Wave Laboratory (SWL) at RWTH Aachen University. In this section, we present numerical 2D results of simulated cooling gas injection into a hot gas supersonic nozzle flow. At first, the experimental setup is briefly described in Sec. 4.1, followed by the numerical setup in Sec. 4.2 and the simulation results in Sec. 4.3.

4.1 Experimental Setup

Transpiration cooling experiments are performed using an axisymmetric conical nozzle with a divergent half-opening angle of 15°, an expansion part of 340 mm and a throat diameter of 16 mm, as illustrated in Fig. 2. To generate a rocket-engine-like nozzle flow the axisymmetric nozzle is attached to a detonation tube. The detonative combustion of a mixture of H2/O2 and the deceleration of these gases to $\mathbf{v} = \mathbf{0}$ in the nozzle plenum chamber provides high pressures and temperatures for a short testing time. The stagnation conditions can be adjusted by the initial conditions of the detonative combustion, namely: gas mixture, temperature and pressure.[27]
The permeable C/C material is mounted in a slot into the nozzle wall starting 98 mm downstream of the throat with a length of 100 mm and a width of 10 mm. The height of the sample is 10 mm. Downstream of the sample measurements of static pressure and heat flux are taken.
To guarantee steady coolant flow during the whole testing time (5-10 ms) the coolant injection starts 35 ms before the hot gas flow arrives.

4.2 Numerical Setup

For first investigations we consider a simplified configuration. Instead of the rotational symmetric experimental setup we confine ourselves to a 2D configuration. Thus, the nozzle area in the cross-section of our 2D setting is linearly increasing whereas in the experiment it increases nonlinearly. Therefore, we cannot directly compare our results to experimental data.

DOI: 10.13009/EUCASS2019-91

Table 2: Coolant parameters.

coolant mass flow rate	$\dot{m}_c$	1.484	g/s
reservoir pressure	p_R	900000	Pa
coolant reservoir temp.	$T_{f,R}$	500	K
backside temperature	$T_{s,R}$	550	K

Table 3: Porous medium parameters.

porosity	φ	0.1111	
solid heat conductivity	κ_s	14.59	W/(m K)
permeability	K_D	$3.57 \cdot 10^{-13}$	m^2
Forchheimer coefficient	K_F	$5.17 \cdot 10^{-8}$	m
heat transfer coefficient	h	$1 \cdot 10^6$	W/(m^3 K)

Nozzle flow: The hot gas domain Ω_{HG} is chosen as the 2D cross-section of the divergent part of the conical nozzle in Figure 2. In contrast to this figure we align the bottom wall with the x-axis. Then the trapezoidal domain is given by the edges $\overline{AB}$, $\overline{AC}$, $\overline{CD}$ and $\overline{BD}$ determined by the points $A = (0\,\text{m}, 0\,\text{m})$, $B = (0.352\,\text{m}, 0\,\text{m})$, $C = (-0.00141\,\text{m}, 0.015455\,\text{m})$ and $D = (0.300702\,\text{m}, 0.191446\,\text{m})$. The computational domain Ω_{HG} is discretized by an initial coarse grid of 40×10 cells where the grid lines are concentrated near the walls and the entry. It is locally refined by at most $l = 10$ refinement levels during the computation.
Air (N2, O2) in the nozzle is initialized as a mixture of molecular nitrogen and oxygen $X_{N_2,\infty} = 0.746$ and $X_{O_2,\infty} = 0.25$. Note that we account for spurious contributions of the other species (N, O, NO, AR) to avoid "vacuum" of these species in the computation. The molar weights of the species are: $M_{N_2} = 28.013$ g/mol, $M_{O_2} = 31.999$ g/mol, $M_N = 14.0065$ g/mol, $M_O = 15.9995$ g/mol, $M_{NO} = 30.006$ g/mol and $M_{AR} = 39.948$ g/mol. The flow conditions for the nozzle flow are listed in Tab. 1.
Porous medium flow: The porous medium domain Ω_{PM} is attached to the bottom nozzle wall from $x = 0.0957$ m to $x = 0.1957$ m as indicated in Fig. 4. It is given by $\Omega_{PM} = 100$ mm $\times$ 10 mm and discretized by a grid with 240×40 cells where the grid lines are concentrated towards both the hot gas and the reservoir side by applying a stretching technique. At the interface to the hot gas flow the first layer of grid cells is refined twice.
The cooling gas is initialized with mass fraction $X_{AR} = 0.995$. Again, we account for spurious contributions of the other species (N, N2, O, O2, NO) to avoid "vacuum" of these species in the computation.
The boundary conditions, see Tab. 2, and the porous medium parameters, see Tab. 3, are chosen in agreement with the planned experiments. Since we perform a steady state computation in both the nozzle as well as the porous medium, the sample will heat up due to heat conduction at the hot gas interface. As we do not account for a heat transfer between the coolant reservoir and the porous sample, both the coolant reservoir temperature and the porous material backside temperature are assumed to be higher than in the planned experiment. We emphasize that due to the short duration of the experiment the porous medium will not heat up. To model this correctly, a transient computation has to be performed.

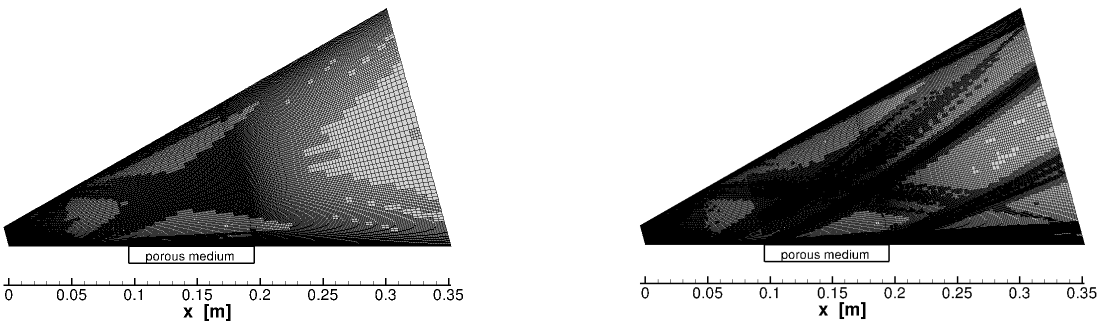

(a) Without cooling gas injection (Step A).

(b) Coupled simulation (Step B).

Figure 3: Locally refined grid.

DOI: 10.13009/EUCASS2019-91

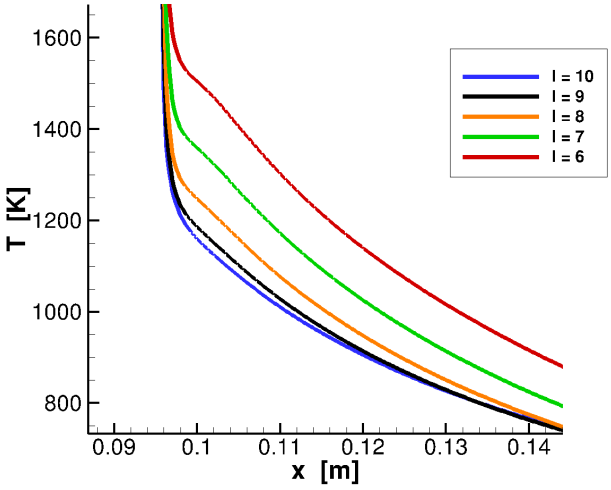

Figure 4: Grid convergence at the leading edge.

To perform a coupled fluid-porous medium computation we proceed in two steps: **Step A:** We first perform a steady state computation of the nozzle flow **without** coupling with the porous medium (neglect Step 2-4 in Algorithm). For computing a stationary solution with the flow solver, an implicit backward Euler time integration scheme is used with local time steps determined by a global CFL number. The following CFL evolution strategy

$$CFL_{n+1} = min(CFL_{min} \cdot 1.01^n, CFL_{max}) \tag{32}$$

is used with the parameters $CFL_{min} = 0.1$ and $CFL_{max} = 50$. Here, the index n enumerates the number of time steps since the last grid adaptation. Grid adaptation is performed whenever the normalized average density residual has dropped to 10^{-4}. Using four grid adaptations with $l = 4$ refinement levels this leads to an adaptive grid with about 85000 cells, see Fig. 3(a). Note that the solution of the uncoupled nozzle flow needs not to be converged. This solution is only used to initialize the coupled computation. **Step B:**The steady state solution is then used to initialize the **coupled** computation. We alternately solve the nozzle flow and the porous medium flow according to Steps 2-7 of the Algorithm with $\varepsilon = 10^{-2}$. Six couplings and grid adaptations are performed leading to a final grid with $l = 10$ refinement levels of about 900000 cells, see Fig. 3(b). Figure 4 shows grid convergence at the trailing edge where the cooling film develops and where the largest temperature differences between the refine levels occur. Here, the difference between the results corresponding to computations with $l = 9$ and $l = 10$ refinement levels is at most 2.5 % and is therefore considered to be sufficiently small. In the last coupling 13 iterations are needed to determine $p_{R,num} = 688039Pa$ with $\|\dot{m}_c - \dot{m}^i_{\text{Int}}\| \leq 2 \cdot 10^{-6}$.

4.3 Simulation Results

In this section, we present the distribution of several quantities in the hot gas flow and in the porous material provided by the two-dimensional simulations.
Step A: The simulation of the supersonic nozzle flow without coupling exhibits two characteristic features, namely, the boundary layer at the walls and two Prandtl-Meyer expansion fans originating at the nozzle entry which are reflected at the walls. These flow structures are clearly visible in the Mach number distribution shown in Fig. 5(a). They are adequately resolved and automatically detected by the grid adaptation procedure, see Fig. 3(a). The Mach number increases from 1 at the nozzle entry to about 3.7 at the nozzle exit.
Step B: When the steady state nozzle flow is coupled with the porous medium a strong effect from the injection can be observed. Due to the injection of cooling gas a cooling film develops on the sample and in its wake. This can be seen in Fig. 6 where the mass fraction of the coolant argon is shown. The injected cooling gas is an obstacle for the hot gas flow. This causes a compression shock wave at the leading edge of the porous sample and an expansion wave at its trailing edge. The latter has to detach above the sample leading to a high wall-normal momentum. This can been seen in Fig. 7 where the wall-normal momentum is presented. Both the compression shock and the expansion wave are adequately resolved as can be seen in Fig. 3(b). They are interacting with the reflected Prandtl-Meyer expansions as can be deduced by comparing Figures 3(a) with 3(b) as well as 5(a) with 5(b).

DOI: 10.13009/EUCASS2019-91

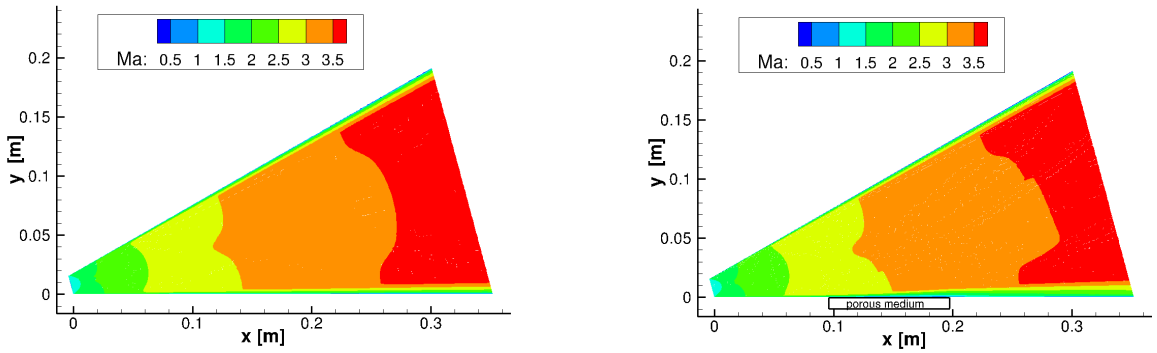

(a) Without cooling gas injection (Step A).

(b) Coupled simulation.

Figure 5: Mach number distribution in the nozzle.

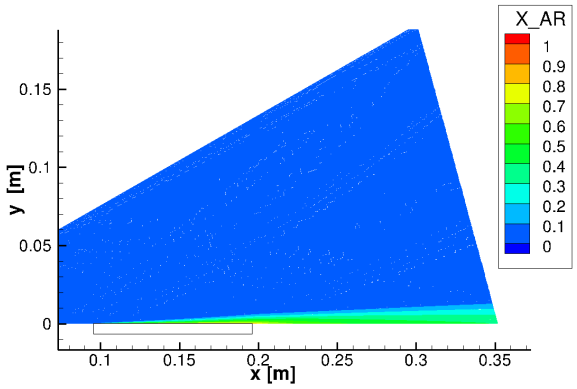

Figure 6: Mass fraction of argon in the nozzle flow.

Of particular interest is the cooling effect at the wall. For this purpose in Fig. 9 we compare the temperature profiles in wall normal direction at different positions on top of the sample (x= 0.137 m and x=0.191 m) and downstream (x= 0.263 m and x=0.346 m) of the sample with those for the non-cooled nozzle. Since the wall is adiabatic, without cooling gas injection the temperature at the wall slightly exceeds the stagnation temperature of $T_\infty = 3486$ K. A coolant film created by the injection through the porous material with increasing thickness over the length of the sample leads to a temperature drop near the wall.

In Fig. 8(a), for position $x = 0.137$ m one can observe a cooling starting 1.4 mm above the wall leading to a wall temperate of 780 K. For position $x = 0.191$ m (close to the trailing edge) the temperature reduction already starts 2.8 mm above the wall and results in 580 K at the wall. In the wake of the sample, see Fig. 8(b), the temperature shows adiabatic behavior. With temperatures between 2700 K and 2900 K the wall is cooler than without cooling gas injection.

We compare the temperature along the nozzle wall without and with cooling gas injection in Fig. 9. The temperatures match in front of the cooling gas injection. Correspondingly to the injection of argon (high concentration above the sample) the temperature drops above the porous medium. Since the cooling film thickens in streamwise direction the temperature is lowest at the trailing edge. Due to mixture processes the concentration of argon drops rapidly in the wake of the porous sample leading to a rise in the temperature. Since argon gets transported along the nozzle wall, the wall temperature of the cooled wall does not return to the non-cooled state, see also Fig. 6.

The coupling of the nozzle with the porous medium also affects the flow in the porous material. We note that the converged value of the reservoir pressure is about $p_{R,num} = 688000Pa$. The pressure difference between Γ_R and Γ_{Int} is the driving force for the porous medium flow. In Fig. 10(a) the density distribution is shown in the porous material. Due to higher pressure (7 bar) in the coolant reservoir and lower pressure in the hot gas flow (0.3 – 0.7 bar), the density evolves from higher values in the coolant reservoir to lower values on the hot gas side. In Fig. 10(b) the temperature of the coolant inside the porous material is shown. At the coolant reservoir the coolant enters the porous material. On

DOI: 10.13009/EUCASS2019-91

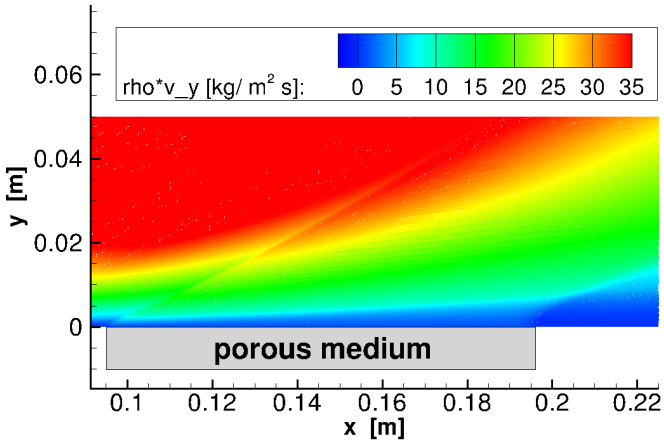

Figure 7: Wall-normal momentum in the nozzle flow.

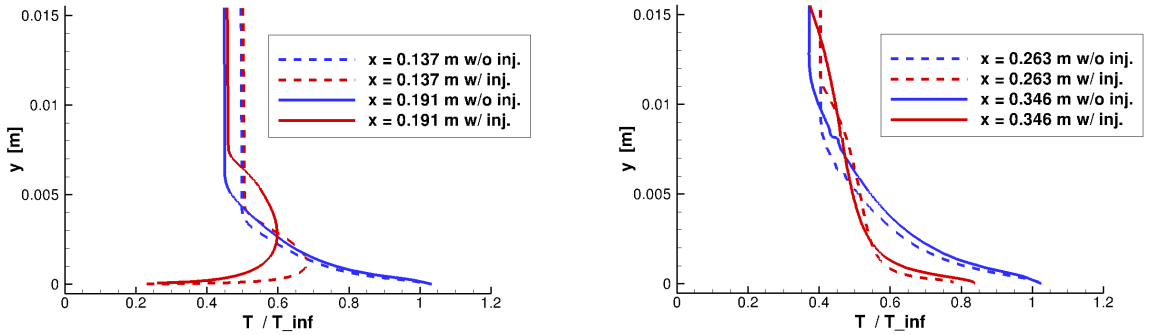

(a) Above the porous material.

(b) In the wake of the porous material.

Figure 8: Temperature profiles in the nozzle.

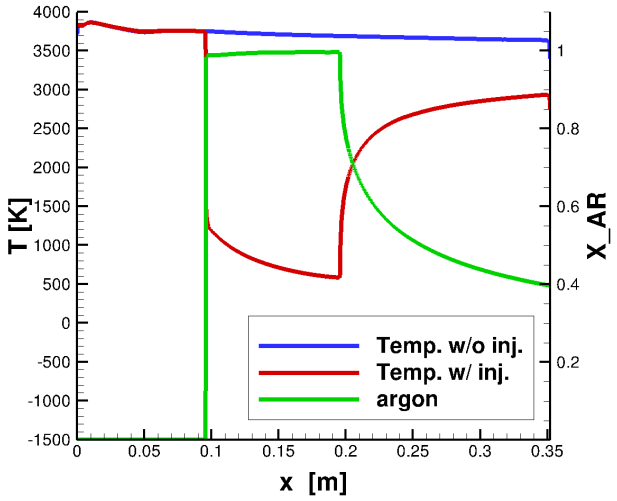

Figure 9: Temperature and mass fraction of argon in the nozzle flow.

DOI: 10.13009/EUCASS2019-91

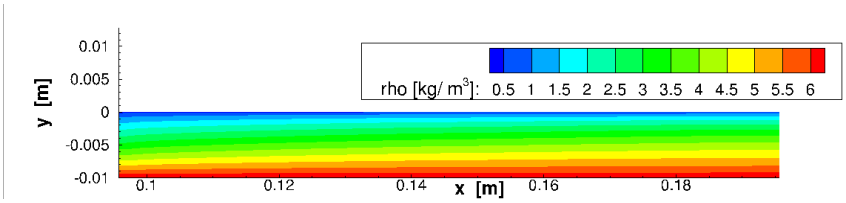

(a) Density distribution of the cooling fluid.

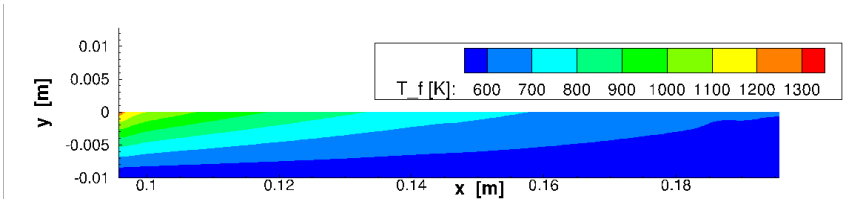

(b) Temperature distribution of the cooling fluid.

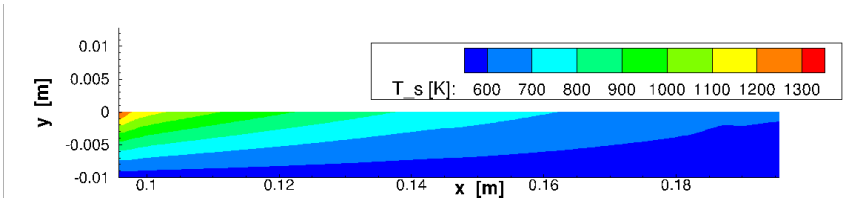

(c) Temperature distribution of the solid material.

Figure 10: Porous medium flow.

its way through the porous wall it absorbs heat from the structure. We observe a strong heating of the structure near to the trailing edge of the coupling interface whereas the structure is cooler further downstream due to the developing coolant film. Since the temperature of the solid is strongly coupled with the temperature of the fluid due to the high heat transfer coefficient h, see Tab. 3, the two temperatures show essentially the same behavior, as can be concluded from Fig. 10(b) and Fig. 10(c). Obviously, there is a strong two-dimensional effect that makes a two-dimensional model mandatory.

In Fig. 6 the highest concentration of argon can be found directly above the porous material at the trailing edge. This corresponds to the significant pressure drop in the nozzle along the interface Γ_{Int}, see Fig. 11. Due to the drop of the pressure gradient between Γ_{Int} and Γ_R in streamwise direction of the nozzle the cooling gas is injected with increasing velocity along the porous material interface.

The profiles of the Darcy velocity for the position $x = 0.11$ m, $x = 0.16$ m and $x = 0.1975$ m near the interface are shown in Fig. 12. Due to the pressure drop in streamwise direction in the nozzle observed in Fig. 11, the velocity at the interface increases from 5 m/s near the leading edge at $x = 0.11$ m to 7 m/s at the trailing edge at $x = 0.1975$ m.

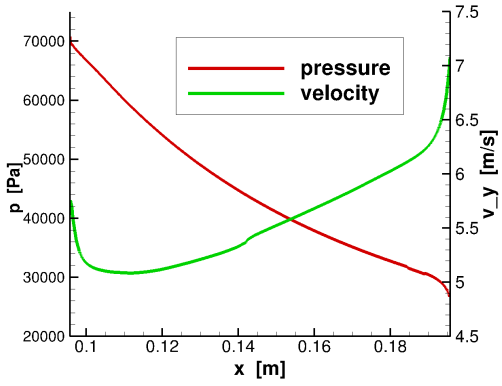

Figure 11: Pressure and wall-normal velocity in the nozzle flow at the interface Γ_{Int}.

DOI: 10.13009/EUCASS2019-91

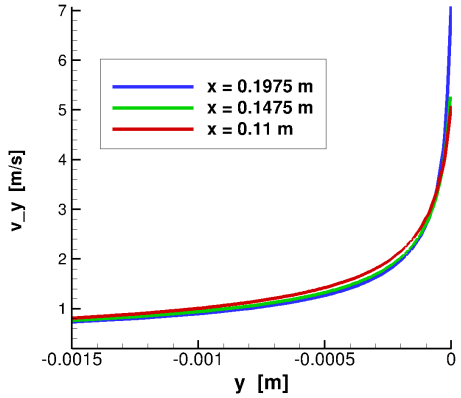

Figure 12: Profiles of Darcy velocity in streamwise direction in the porous medium flow.

5. Conclusions

In previous work,[6,9] the coupled two-domain approach to simulate transpiration cooling in a subsonic channel was investigated. Herein moderate temperatures of about 500 K were considered. A validation of this model was performed using experimental results for a uniform[7] and non-uniform injection.[14]
This approach is now applied to numerically investigate transpiration cooling in a supersonic nozzle flow with a mixture of frozen gases. Temperatures up to 3500 K and large pressure gradients are used to account for realistic nozzle conditions. Transpiration cooling with argon as the coolant shows to be efficient to reduce the heat fluxes at the wall of the nozzle.
Compared to the hot gas channel setup, where the difference between cooling gas and hot gas was around 100 K, for the nozzle flow the difference exceeds 3000 K. The pressure drop along the interface of the porous medium sample leads to an increase of the mass flow rate in streamwise direction. Here the usage of several segments of porous media with different porosities and therefore mass flow rates might be superior to the current approach of using only one sample.
In the future we would like to extend our numerical investigations of cooling a hot nozzle by using helium as a coolant as will be used in the experiments. Since helium has a lower molecular weight than argon, a thicker cooling film will develop at the same mass flow rate reducing the temperature gradient and, thus, causing a lower heat load to the structure. This has already been observed in investigations of film cooling in a supersonic channel, see.[26] Comparisons to experiments performed by the SWL Aachen are a long term goal.

Acknowledgments

Financial support has been provided by the German Research Foundation (Deutsche Forschungsgemeinschaft – DFG) in the framework of the Sonderforschungsbereich Transregio 40.

References

[1] W. Bangerth, R. Hartmann, and G. Kanschat. deal.ii - a general-purpose object-oriented finite element library. *ACM Transactions on Mathematical Software*, 33(4):24/1–24/27, 2007.

[2] R.B. Bird, W.E. Stewart, and E.N. Lightfoot. *Transport Phenomena*. John Wiley & Sons, Inc., 2007.

[3] F. Bramkamp, P. Lamby, and S. Müller. An adaptive multiscale finite volume solver for unsteady and steady state flow computations. *Journal of Computational Physics*, 197(2):460–490, 2004.

[4] L.D. Cloutman. A database of selected transport coefficients for combustion studies. Technical report, Lawrence Livermore National Laboratory, 1993.

[5] W. Dahmen, V. Gerber, T. Gotzen, S. Müller, M. Rom, and C. Windisch. Numerical simulation of transpiration cooling with a mixture of thermally perfect gases. In *Proceedings of the jointly organized WCCM XI - ECCM V - ECFD VI 2014 Congress, Barcelona*, pages 3012–3023, 2014.

DOI: 10.13009/EUCASS2019-91

[6] W. Dahmen, T. Gotzen, S. Müller, and M. Rom. Numerical simulation of transpiration cooling through porous material. *International Journal for Numerical Methods in Fluids*, 76(6):331–365, 2014.

[7] W. Dahmen, S. Müller, M. Rom, S. Schweikert, M. Selzer, and J. v. Wolfersdorf. Numerical boundary layer investigations of transpiration-cooled turbulent channel flow. *International Journal of Heat and Mass Transfer*, 86:90–100, 2015.

[8] E.R.G. Eckert and J.N.B. Livingood. Comparison of effectiveness of convection-, transpiration-, and film-cooling methods with air as coolant. Report 1182, National Advisory Committee for Aeronautics, 1954.

[9] T. Gotzen. *Numerical Investigation of Film and Transpiration Cooling*. PhD thesis, RWTH Aachen University, 2013.

[10] A. Herbertz and M. Selzer. Analysis of coolant mass flow requirements for transpiration cooled ceramic thrust chambers. *Trans. JSASS Aerospace Tech. Japan*, 12(29):31–39, 2014.

[11] J.O. Hirschfelder, C.F. Curtiss, and R.B. Bird. *Molecular Theory of Gases and Liquids*. John Wiley & Sons, Inc., 1965.

[12] P. Jiang, L. Yu, J. Sun, and Y. Wang. Experimental and numerical investigation of convection heat transfer in transpiration cooling. *Applied Thermal Engineering*, 24:1271–1289, 2004.

[13] D Keener, J Lenertz, R Bowersox, and J Bowman. Transpiration cooling effects on nozzle heat transfer and performance. *Journal of Spacecraft and Rockets*, 32(6):981–985, 1995.

[14] V. König, M. Rom, S. Müller, S. Schweikert, M. Selzer, and J. v. Wolfersdorf. Numerical and experimental investigation of transpiration cooling with C/C characteristic outflow distributions. *Journal of Thermophysics and Heat Transfer*, 33(2):449–461, 2019.

[15] Jay Landis and W Bowman. Numerical study of a transpiration cooled rocket nozzle. In *32nd Joint Propulsion Conference and Exhibit*, page 2580, 1996.

[16] T. Langener. *A Contribution to Transpiration Cooling for Aerospace Applications Using CMC Walls*. PhD thesis, Stuttgart University, 2011.

[17] T. Langener, J. v. Wolfersdorf, M. Selzer, and H. Hald. Experimental investigations of transpiration cooling applied to C/C material. *International Journal of Thermal Sciences*, 54:70–81, 2012.

[18] F.R. Menter. Two-equation eddy-viscosity turbulence models for engineering applications. *AIAA Journal*, 32(8):31–39, 1994.

[19] D. A. Nield and A. Bejan. *Convection in Porous Media*. Springer, 2006. 3rd ed.

[20] M. Ortelt, H. Hald, A. Herbertz, and I. Müller. Advanced design concepts for ceramic thrust chamber components of rocket engines. In *5th European Conference for Aeronautics and Space Sciences (EUCASS), Munich*, 2013.

[21] Daniel Prokein and Jens von Wolfersdorf. Numerical simulation of turbulent boundary layers with foreign gas transpiration using OpenFOAM. In *7th European Conference for Aeronautics and Space Sciences (EUCASS), Milan*, 2017. doi:10.13009/EUCASS2017-589.

[22] M. Selzer, T. Langener, H. Hald, and J. v. Wolfersdorf. Production and characterization of porous C/C material. Annual Report SFB TRR40 2009. Munich.

[23] D.R. Stull and H. Prophet. Janaf thermochemical tables [electronic source]. Technical report, National Institute of Standards and Technology, 2011.

[24] John E Terry and Gus J Caras. Transpiration and film cooling of liquid rocket nozzles. Technical report, REDSTONE SCIENTIFIC INFORMATION CENTER REDSTONE ARSENAL AL, 1966.

[25] F. M. White. *Fluid Mechanics*. McGraw-Hill, 2009.

[26] C. Windisch. *Efficient Simulation of Thermochemical Nonequilibrium Flows using Highly-Resolved h-adapted Grids*. PhD thesis, RWTH Aachen University, 2014.

[27] G. Yahiaoui and H. Olivier. Development of a short-duration rocket nozzle flow simulation facility. *AIAA Journal*, 53(9):2713–2725, 2015.